CHAPTER-VI

OPTICALLY SEE-THROUGH EMBEDDED DEEP EUTECTIC SOLVENT GEL META-STRUCTURE ABSORBER

References

6.1 INTRODUCTION

Optically see-through absorbing material enables camouflaging EM signature without compromising on optical visibility and aesthetics. Such materials can be integrated with window shields, radomes, solar panels or electronic toll systems etc., where transparency in visible range is desired along with microwave shielding. Compounding both optical transparency and good shielding for absorbers set limits on choice of materials and designs. Demand for flexibility and broad absorption bandwidth has further augmented design and fabrication intricacies on the optically transparent absorbers.

The development of an optically transparent flexible MSA requires mainly three prerequisites: 1) an optically transparent resonator, 2) an optically transparent matrix and 3) an optically transparent conducting back with sufficient flexibility, none of which can be compromised. Research on MSAs with good optical transparency has thus been limited or rather hardly reported.

DES gel, used in the chapters IV and V, demonstrates favourable microwave properties as resonating structures for developing wide band flexible MSAs. It has a pale-yellow hue and optical transmittance measurement shows sufficient transparency in the visible range, Figure 6.1, with values tabulated in Table 6.1.

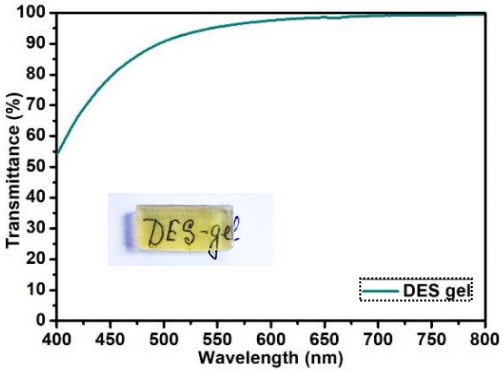

Figure 6.1 Transmittance curve of DES gel at optical frequencies, inset: optical image DES gel.

Table 6.1 Optical properties of DES gel.

Material parameter	*Value*	*Equipment*
Optical transmittance (%)	55-80% from λ = 400-500 nm, >80% for λ >500 nm	UV-visible spectrometer (Perkin Elmer-Model: UV/VIS Lambda 365)

The silicone rubber matrix used in previous studies is to be replaced by an optically transparent hydrophobic alternative having similar flexibility. Urethane rubber - a

polyurethane elastomer, (datasheet attached as appendix I) is an optically transparent polymer which like silicone rubber is easily castable at room temperature. It is also flexible and lightweight. Urethane rubber is used in maritime applications indicating its sufficient water resistance and low moisture uptake [1, 2].

Subsequently, replacement of reflective metallic backs in MSAs would enable to meet the third essential requirement. Indium tin oxide (ITO) [3-12] and graphene [13-17], are reported as transparent substitute to metallic conducting/reflecting back. However, processing multi-layered ITO and graphene for obtaining optimum conductivity has its own fabrication complexity [18]. Further, these structures are constraint by limited flexibility.

Another alternative is using metallic mesh, which has been utilised more frequently for shielding EM waves ever since the "Faraday cage" effect was discovered in 1836 [19, 20]. It acts as subwavelength structure to microwave resulting in reflection and as macroscopic structure to infrared and visible frequency ranges resulting in transmission[21-23]. Thus, at the same time passing the visible range and blocking off the microwave range.

In this chapter, an optically transparent DES gel meta-structure absorber (OT-MSA) is designed and optimized to transmit the visible frequency range while attenuating the X-band. The developed transparent absorber is tested for its absorption and RCS performance. Further, an investigation is carried out to test its application on camouflaging solar panel.

6.2 PREPARATION AND CHARACTERIZATION OF URETHANE RUBBER

6.2.1 Preparation

Urethane rubber is processed from urethane rubber viscous gel (Clear Flex-50 from Smooth-on, Inc.) component A and B mixed in 2:1 weight (wt.) ratio. The mixture is mixed well and then de-aerated inside vacuum pump (~60 Pa) to eliminate any entrapped air bubbles from the viscous mixture. It is then poured onto desired sized/shaped mould of silicone rubber and left undisturbed for 6 h at room temperature. Thereafter heat treated at ~65˚C for complete curing. The schematic in Figure 6.2 shows the general preparation process of urethane rubber.

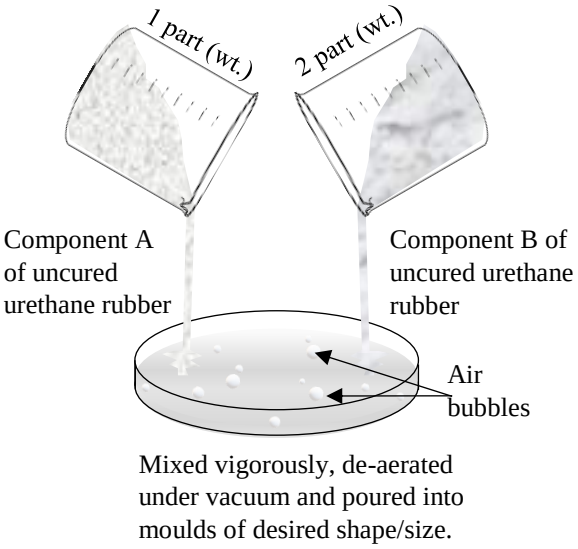

Figure 6.2 Schematic of the synthesis process of urethane rubber.

6.2.2 Characterization

The prepared urethane rubber is characterized for its material as well as microwave properties, Figure 6.3(a)-(f). The results are presented in Table 6.2.

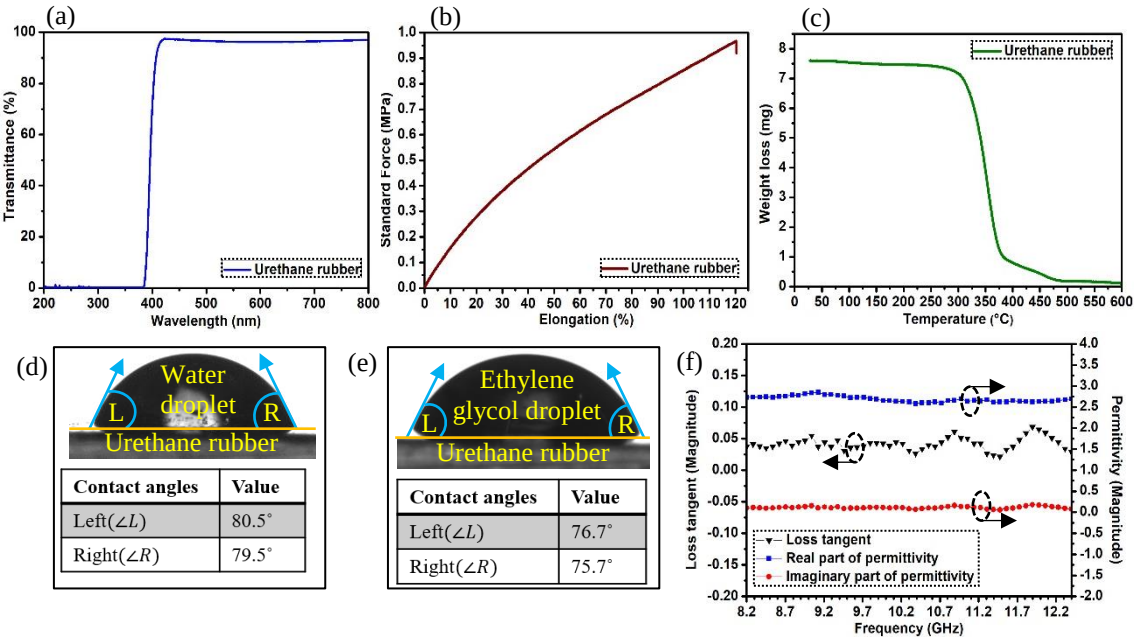

Contact angles	Value
Left($\angle L$)	80.5°
Right($\angle R$)	79.5°

Contact angles	Value
Left($\angle L$)	76.7°
Right($\angle R$)	75.7°

Figure 6.3 (a) Transmittance curve at UV-visible range, (b) tensile strength, (c) TGA curve of the processed urethane rubber. Contact angles of urethane rubber formed with (d) water and (e) ethylene glycol. (f) Complex permittivity values of the urethane rubber in X-band.

Table 6.2 Material properties of synthesized urethane rubber.

Material parameter	*Values*	*Equipment/method used*
Optical transmittance	≥ 98% (from λ = 400 - 800 nm) [**Figure 6.3(a)**]	UV-visible spectrometer (Perkin Elmer-Model: UV/VIS Lambda 365)
UV transmittance	~0% (from λ =200 - 400 nm) [**Figure 6.3(a)**]	UV-visible spectrometer (Perkin Elmer-Model: UV/VIS Lambda 365)
Tensile strength	~0.95 MPa [**Figure 6.3(b)**] with maximum elongation=120%	5KN Electro mechanical Universal Testing Machine, Make: Zwick Roell, Model: Z005TN Proline
Decomposition temperature	~300˚C [**Figure 6.3(c)**]	Thermogravimetric analyzer (SHIMADZU-Model: TGA 50)
Wettability (Contact angles with water)	≥ 79˚ [**Figure 6.3(d)**]	Contact angle measurement system. (Data physics GmbH, Model: OCA 15 EC)
Water absorbance*	2.6%	$\frac{Weight_{submergered} - Weight_{actual}}{Weight_{actual}} \times 100\%$
Wettability (Contact angles with ethylene glycol)	≥ 75˚ [**Figure 6.3(e)**]	Contact angle measurement system. (Data physics GmbH, Model: OCA 15 EC)
Ethylene glycol absorbance*	0.94%	$\frac{Weight_{submergered} - Weight_{actual}}{Weight_{actual}} \times 100\%$
Density	1.0774 g cm^{-3}	Archimedes' principle
Complex permittivity	$2.9 \pm j0.1$ (at X-band) [**Figure 6.3(f)**]	Keysight N1501A dielectric probe with an Agilent Vector Network Analyzer E8362C (VNA)
Note: *Water and ethylene glycol absorbance is checked by submerging the sample for 72 hrs and measuring change in weight.		

The synthesized urethane rubber shows opacity in UV range and a good transparency in the visible range. It shows high tensile strength indicating good flexibility. The high decomposition temperature makes it stable upto ~350˚C. Urethane rubber displays contact angles $< 90°$ both with water and ethylene glycol, indicating that the resonators of DES gel when embedded in this substrate will experience lower slippage as compared to silicone rubber. Low water and ethylene glycol absorptivity makes it almost resistant to both the liquids. Urethane rubber has low dielectric loss over the entire X-band. Combination of high lossy sub-wavelength resonator with the low loss matrix will result in matching of the impedance at the air-MSA interface. Thus, urethane rubber exhibits all the desired characteristics for the development of optically clear and flexible matrix for MSAs.

6.3 DESIGN AND SIMULATION OF COPPER MESH BACKED OT-MSA

The design simulation is carried out in two steps (1) optimization of the unit cell structure to obtain a broad absorption bandwidth and (2) mesh size alteration to get

good optical transparency along with minimum microwave transmittance. Vector fields associated with the absorption mechanism of the structure are later analysed.

6.3.1 Unit cell structure design

The layout of the unit cell is a cuboidal urethane rubber substrate with subwavelength hexagonal-prism shaped DES gel resonator which shows 6-fold symmetry for polarization independent performance as drawn in Figure 6.4(a). The dimensions of the structure are optimized around the central frequency (~10.3 GHz) of the X-band. The cuboidal substrate dimensions are fine-tuned to reduce cross-coupling between the resonators. A thin layer of urethane rubber is laid on the top of the unit cell to prevent degradation of embedded DES gel. All structural optimizations are initially conducted with the assumption that the MSA is backed with a copper sheet. Later, the metallic back is replaced with a copper mesh as redrawn in Figure 6.4(b)-(d) and mesh size optimizations is carried out as discussed in the following section. The schematic of proposed copper mesh backed OT-MSA is given in Figure 6.4(e). All simulations are conducted using Floquet port in Frequency Domain Solver on the CST Studio Suite software, Figure 6.4(f). The finalized values of the MSA unit dimensions are given in Table 6.3.

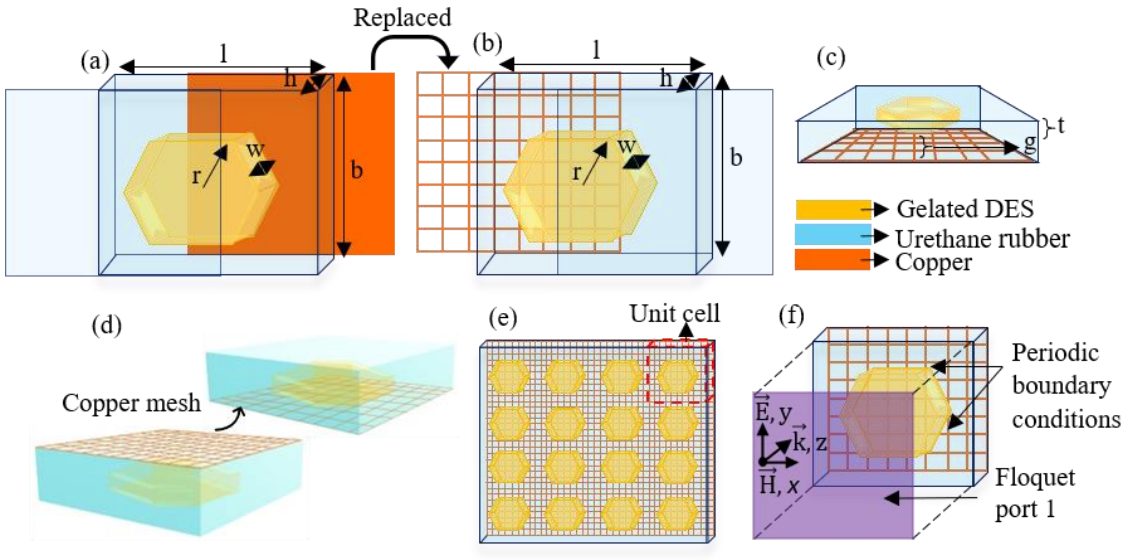

Figure 6.4 Schematic of OT-MSA (a) unit cell backed with copper, (b) unit cell backed with copper mesh, (c), (d) copper mesh backed unit cell side view. Schematic of the copper mesh back MSA (e) proposed MSA and (f) unit cell with Floquet port.

Table 6.3 Optimized parameters of OT-MSA.

Dimension	Description	Value (mm)
l	Length of the substrate	9.6
b	Breadth of the substrate	9.6
h	Height of the substrate	3.2
w	Thickness of the resonator	1.5
r	Radius of the resonator	4
g	Substrate layer thickness below resonator	1.5
t	Substrate layer thickness above resonator/ Cover	0.2
	Copper thickness	0.035
	Copper mesh thickness	0.15

6.3.2 Mesh size optimization

Metallic mesh coatings have been demonstrated as a reflecting back for optically transparent microwave absorbers in papers [15, 18, 24, 25], wherein the meshes are of nano scaled thickness and fabricated using lithography or sputtering. The development process, however, is intricate and expensive. Furthermore, there is always a possibility of defects in the coating and uniformity of surface resistance. Commercially available near micrometre sized meshes on the other hand are readily accessible and economically viable. In addition, they have adequate flexibility and sufficient optical transparency. Here, copper mesh of micro sized thickness is considered.

The size of reflecting back copper mesh of MSA unit cell Figure 6.4(b)-(d), is optimized to provide sufficient transparency without compromising on the -10 dB absorption bandwidth. The diameter of the copper mesh wire is ~150 µm. Three mesh sizes are considered, 0.5, 1.0 and 1.5 mm. The simulated reflection loss values

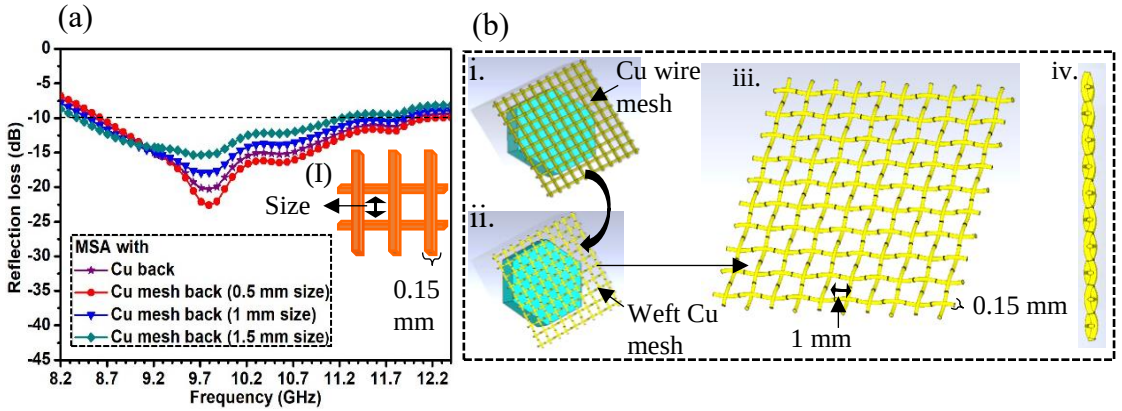

Figure 6.5 (a) Simulated reflection loss values of copper backed OT-MSA and copper mesh backed OT-MSA different mesh sizes and inset I: schematic of the mesh size. (b) Schematic of OT-MSA backed with copper (i) wire mesh and (ii) weft mesh. Copper weft mesh (iii) top view and (iv) side view.

are presented in Figure 6.5(a). The simulated results and respective optical transmittance (calculated) are tabulated in Table 6.4.

Table 6.4 Simulated absorption performance of OT-MSA backed with copper and copper mesh of different sizes.

OT-MSA backed with copper	RF (GHz)	RL (dB)	-10 dB BW (GHz)	*O-T (%)
Sheet	9.79	-20.29	3.3	-
Mesh of size 0.5 mm	9.79	-22.61	3.4	49.4
Mesh of size 1 mm	9.71	-17.94	3.3	71.2
Mesh of size 1.5 mm	9.62	-15.35	2.8	79.3
Weft mesh of size 1 mm	9.71	-18.29	3.3	71.2

Note: RF- Resonant frequency, RL- reflection loss, BW-bandwidth, O-T-optical transparency.

*Optical transparency of mesh = $\frac{Area\ of\ MSA\ (l.b) - Area\ covered\ by\ mesh\ [a(m.l+n.b) - a^2(m.n)}{Area\ of\ MSA\ (l.b)} \times 100\%$ [26]

a=diameter of the mesh, m=no. of mesh lines along length, l, and n= no. of mesh lines along breadth, b.

The absorption bandwidth for 0.5 and 1mm mesh size is found to be akin with the copper backed OT-MSA, while it reduces marginally for 1.5 mm sized mesh. Optical transparency of ~49% is observed for 0.5 mm mesh window while 1 mm and 1.5 mm mesh window show 71% and 79% of transparency respectively. Making the absorber optically see-through requires a trade-off between MSA performance and meshing characteristics. Here, mesh of size 1 mm is chosen for design and development of the proposed MSA.

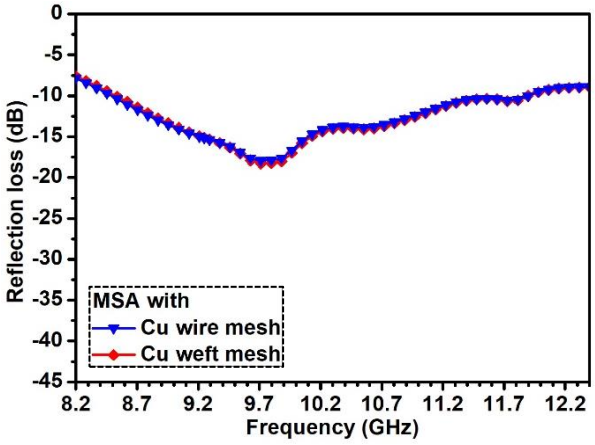

Figure 6.6 Simulated reflection loss values of copper meshed OT-MSA with copper wire mesh and weft mesh.

The simulations are carried out considering mesh as a straight copper wire mesh, however, copper mesh available are mostly weft meshes, Figure 6.5(b). Simulation is carried out with copper weft mesh for mesh size of 1 mm, Figure 6.6 and written in Table 6.3. The results are found to be very close with straight copper wire mesh. Hence, simulation with straight wire mesh are considered for carrying out future

simulations as it is easier to design on simulation software as well as requires less time for complete processing of the results.

6.3.3 Absorption analysis

Plots in Figure 6.7(a) shows simulated values of absorption, transmission and reflection for copper mesh backed OT-MSA in dB and linear scale in inset: (I). From the graphs in Figure 6.7(b), Z_a' approaches unity while Z_a'' approaches zero at 9.71 GHz, where maximum absorption, i.e. $A_\omega \rightarrow 1$, and R_ω and $T_\omega \rightarrow 0$. The effective permittivity and permeability at the maximum absorption point are found to be $(\varepsilon_a) = -3.28 + 13.4$ and $(\mu_a) = 3.32 + 12.4$ respectively, Figure 6.7(c). Negative permittivity indicates the MSA to be single negative metamaterial.

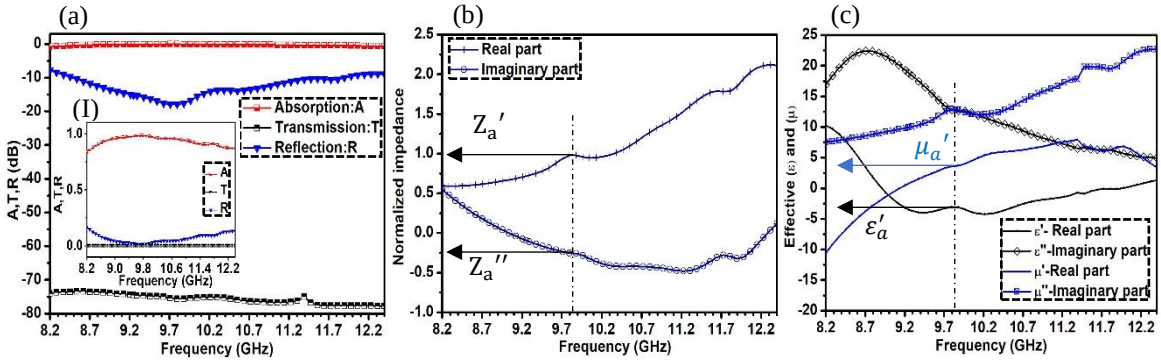

Figure 6.7 Simulated (a) absorption, transmission and reflection loss values, inset (I): in linear scale. (b) normalized impedance, and (c) effective permittivity and permeability of copper mesh backed OT-MSA.

The designed MSA is evaluated for polarization and incidence angular dependency. The structure shows polarization insensitivity upto $\pm 90^\circ$, Figure 6.8(a), and the performance of the MSA shows wide incident angle independency upto $\pm 50^\circ$ in both TE and TM modes as can be seen from Figure 6.8(b) and (c).

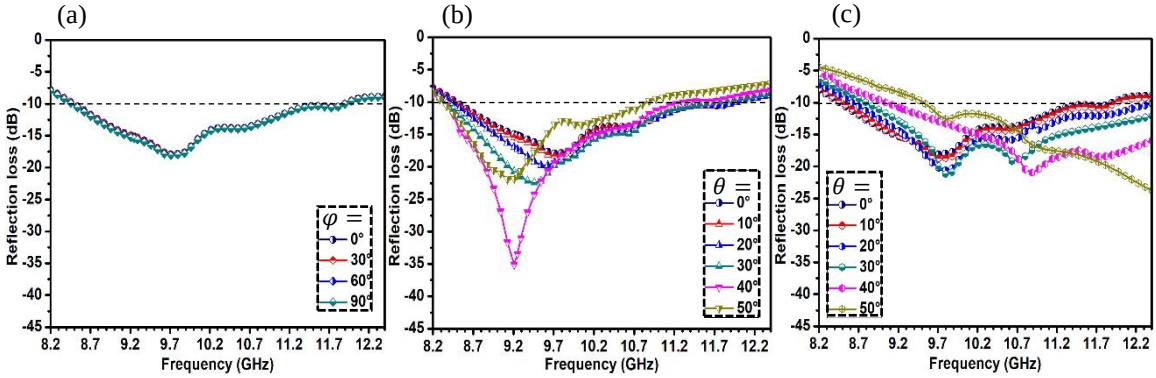

Figure 6.8 Simulated reflection loss with different (a) polarization angles and incident angles in (b) TE mode and (c) TM mode of copper mesh backed OT-MSA.

Field analysis

The E-field is localised predominantly at the edges of the DES gel resonator, Figure 6.9(a), similar to chapters IV and V. The electric field induced and the surface current generated on the metallic mesh give rise to an electric response that adds to the effective permittivity. Concentration of the H-field, as depicted in Figure 6.9(b), is observed at the central region of the DES gel unit and the urethane rubber layer situated above the ground surface. The current density inside the resonator is induced by the incident H-field component, as shown in Figure 6.9(c). The presence of currents throughout the DES gel leads to the occurrence of induction loss or indirect conduction loss, as stated earlier. The power distribution is observed over the entire MSA, Figure 6.9(d), the maximum contribution is from the high dielectric lossy DES gel. All the simulated field distributions are carried out at 9.71 GHz.

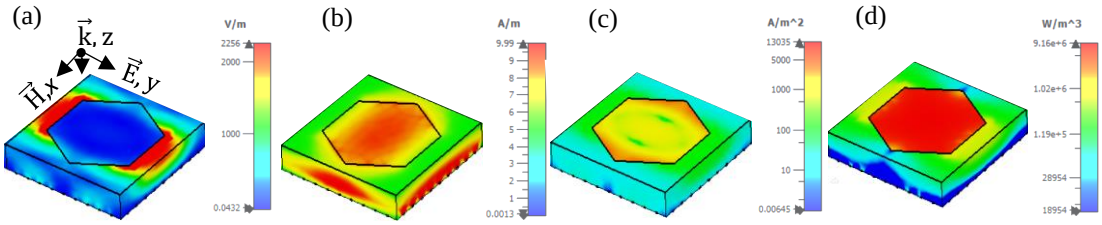

Figure 6.9 Simulated (a) E-field distribution, (b) H-field distribution, (c) induced current density and (d) scattered power density in the copper mesh backed-OT-MSA.

6.4 PERFORMANCE OF THE COPPER MESH BACKED OT-MSA

6.4.1 Fabrication

The fabrication of the MSA is carried out in the following stages: (1) Moulding of matrix using the dimensions from Table 6.3, is done in two phases, first a primary PLA (Polylactic acid) mould is additively manufactured using BoXZY 3D printer, Figure 6.10(a). Since urethane adheres to PLA, a secondary silicone rubber mould is developed using the primary mould, Figure 6.10(b). Urethane rubber mixture is poured into the silicone rubber mould, Figure 6.10(c). Shrinkage of all the polymers are accounted for while moulding. (2) Copper mesh is placed on the flat end of urethane rubber within 2 h of its moulding and is left, thereafter, for another 6-7 h for complete hardening, Figure 6.10(d). For copper-backed MSA, copper tape is pasted after urethane rubber sets completely, Figure 6.10(d'), (3) DES gel is heated upto ~70 ˚C to get a pouring consistency. The hexagonal-prism

shaped grooves are filled with the gel and thereafter cooled upto room temperature, Figure 6.10(e) and (e'). (4) The moulded structure is sealed with thin urethane layer to protect the DES gel from environmental damage, Figure 6.10(f) and (f').

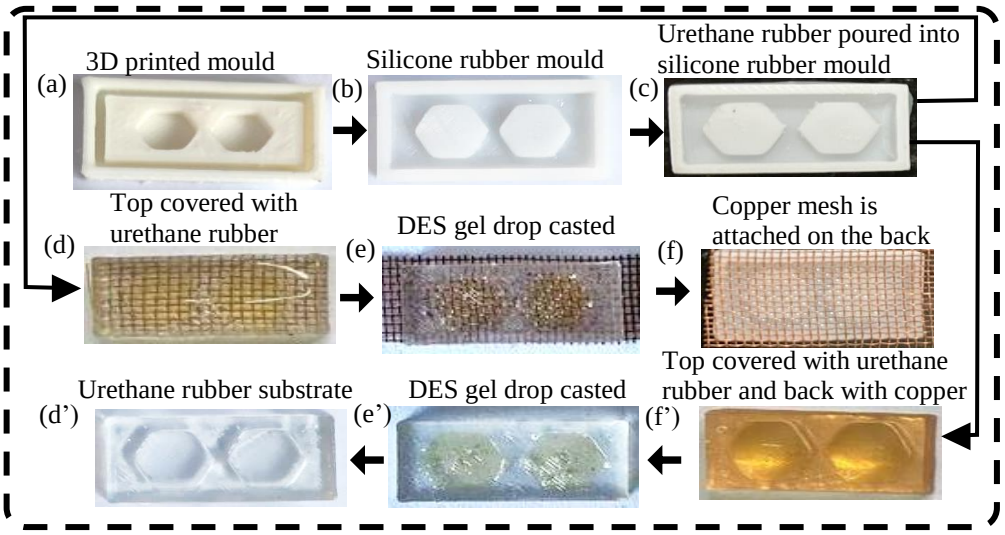

Figure 6.10 Fabrication of the copper backed OT-MSA and Cu mesh backed-OT-MSA.

6.4.2 Mesh adhesion testing

The strength of bonding of copper mesh with urethane is tested in a UTM (model WDW-10, JINAN, CHINA, 1.0 kN load cell and a crosshead speed of 20 mm min^{-1}). The schematic of peeling (adhesion) strength measurement is depicted in Figure 6.11(a) and (b). Mesh shows a good adhesion to urethane rubber with an average elongation of 10%, Figure 6.11(c). The adhesion is comparable with the copper tape backed urethane rubber.

6.4.3 Flexibility testing

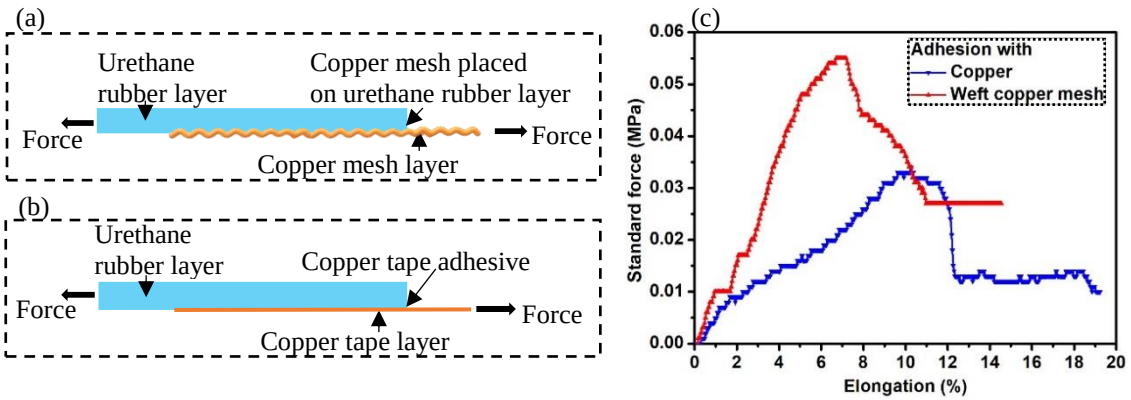

Figure 6.11 Illustration of adhesion (peeling strength) measurement for (a) copper mesh and (b) copper tape with urethane rubber and (c) corresponding peeling strength curves.

The tensile strength of the OT-MSA structure is determined using the above mentioned UTM. The elongation is found to be ~40%, while only urethane shows an elongation of 120%, Figure 6.12(a). The measurement technique is illustrated in Figure 6.12(a) inset:(I).

6.4.4 Examination of optical transparency

The optical transparency is measured in UV-visible spectrometer (Perkin Elmer-Model: UV/VIS Lambda 365). The optical transparency of OT-MSA and copper mesh backed OT-MSA is found to be 80% and 45%, respectively, Figure 6.12(c). Alone copper mesh shows a transparency of 55%.

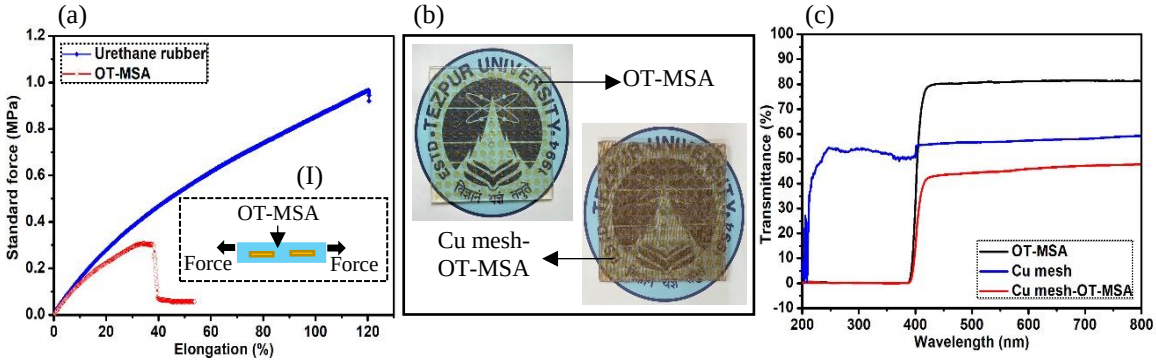

Figure 6.12 (a) Tensile strength of OT-MSA and urethane rubber, inset (I): illustration of tensile measurement technique. (b) Developed 15 X 15 cm^2 OT-MSA and Cu mesh backed OT-MSA. (c) Optical transmittance plots of OT-MSA, copper mesh and Cu mesh backed OT-MSA.

6.4.5 Absorption performance

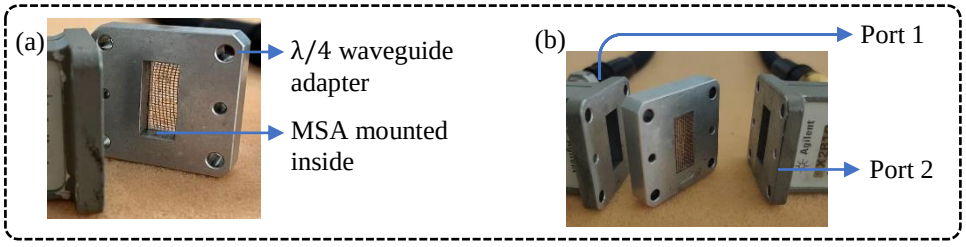

Figure 6.13 (a) Waveguide measurement setup with the mounted sample. (b) Marking the two ports.

Wave guide technique is used to determine absorption performance of the developed copper mesh backed OT-MSA, Figure 6.13. The reflection loss (S_{11}) is measured via port 1 of the VNA. The possibility of any leakages taking place from the mesh back, transmission (S_{21}) is measured through port 2. Plots of the experimental, as well as

simulated reflection loss are presented in Figure 6.14(a). The experimental curve shows a reflection loss of −26.39 dB at 10.04 GHz with a -10dB bandwidth of 3.9 GHz. Hardly any transmission is observed for copper mesh-backed MSA, Figure 6.14(b) indicating effective blocking off microwave. The measured and simulated absorbance curves, Figure 6.14(c), show >80% absorbance for the entire X-band and approaches unity at the resonant frequency.

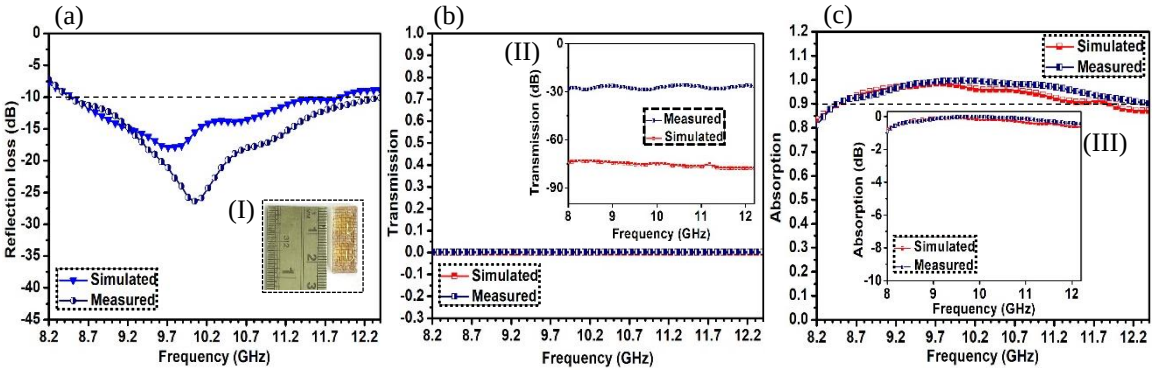

Figure 6.14 Measured (a) reflection loss, (b) transmission and (c) absorption of the copper mesh backed MSA.

The disparities between simulated and experimental absorption results could be because of infinite extent of MSA size which however, is limited in experimental fabrication. The fabrication accuracy is constraint to second decimal place which inadvertently may result in differences observed in simulated and measured results.

6.4.6 Temperature studies

Temperature dependence absorption performance is tested in two different temperature ranges first from room temperature i.e. 25℃ to 65℃ and the other below room temperature down to -15℃.

At higher temperatures, an enhancement is observed in -10 dB absorption bandwidth, Figure 6.15(b). There is a decrease in -10 dB bandwidth, at lower temperatures, Figure 6.15(c). However, the changes in bandwidth are subtle. Possible reasons for these changes could be the temperature dependency of conduction loss and interfacial polarization losses in the gel. When absorber is exposed to higher temperatures, DES gel melts resulting in breakdown of the polymer network which in turn may increase conduction loss while reducing interfacial polarization losses in the gel. In contrast, when the absorber is subjected

to lower temperatures, polymer chains in DES gel may tighten resulting in strong polarization loss while lowering conduction loss.

The reflection loss tends to revert to its original value on bringing the temperature back to room temperature.

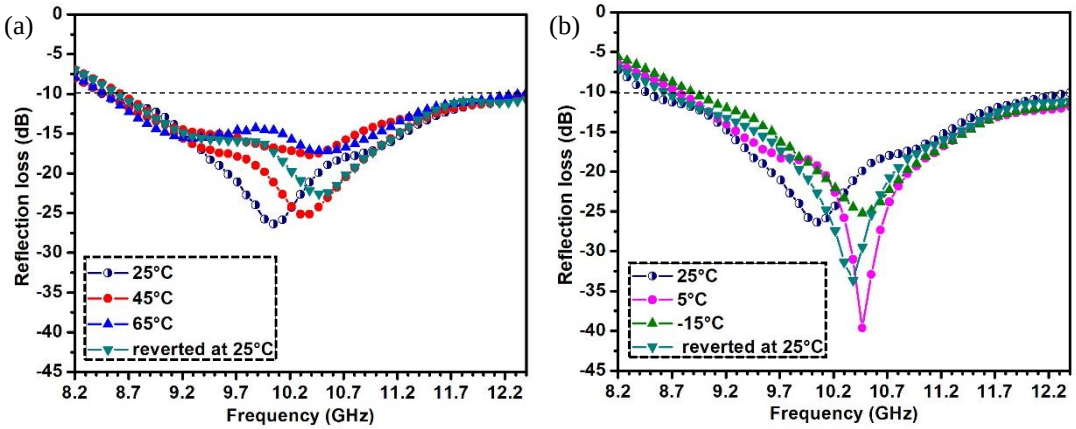

Figure 6.15 Reflection loss values of copper mesh backed OT-MSA at temperatures (a) ≥ 25°C, and (b) ≤ 25°C.

6.5 RCS PERFORMANCE OF COPPER MESH BACKED OT- MSA

6.5.1 RCS Simulation

Both bistatic and monostatic RCS of Cu meshed-OT-MSA of size 15×15 cm^2 $= 5\lambda \times 5\lambda$, with $13 \times 13 = 169$ unit cells are simulated in CST. At first, the bistatic RCS of copper mesh and continuous copper plate of same size is simulated separately, to figure out any discrepancies. Far-field 3D RCS plots for both the copper and copper-mesh, as seen from Figures 6.16(a) and (b), have similar distribution indicating that, while simulation for bistatic mode, copper plate can be considered instead as it will reduce the time of simulation. A notable reduction in bistatic RCS is observed for OT-MSA backed with copper mesh as compared to bare copper plate and copper mesh alone as obvious from the 3D plot Figure 6.16 (c).

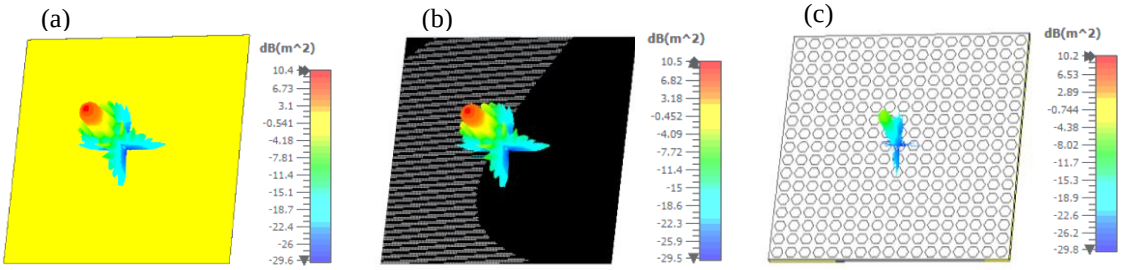

Figure 6.16 Simulated 3D bistatic RCS (a) of copper plate, (b) copper mesh and (c) copper mesh backed OT-MSA.

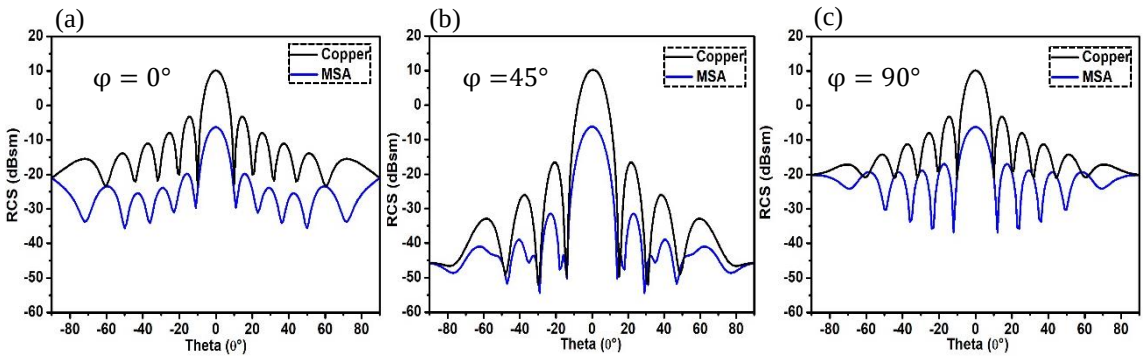

Figure 6.17 Simulated 2D bistatic RCS of copper plate and copper mesh backed OT-MSA with polarization angles (a) 0° , (b) 45° and (c) 90°.

The 2D plots of the bistatic RCS of MSA and reference copper plate are displayed in Figure 6.17 at different polarization angles (φ). The results are tabulated in Table 6.5.

Table 6.5 Bistatic RCS performance of the copper mesh-OT-MSA in reference to copper plate.

Incidence angle	Sample	Bistatic RCS at different polarization angles		
		$\varphi = 0°$	$\varphi = 45°$	$\varphi = 90°$
$\theta = 0°$	Copper plate	10 dBsm	10 dBsm	10 dBsm
	Copper mesh-OT-MSA	-10 dBsm	-10 dBsm	-10 dBsm
$\theta < 0°$ or $\theta > 0°$	Copper plate	≤ -5 dBsm	≤ -10 dBsm	≤ -5 dBsm
	Copper mesh-OT-MSA	≤ -20 dBsm	≤ -15 dBsm	≤ -20 dBsm

The bistatic RCS reduces to more than 20 dBsm at normal incidence i.e. at $\theta = 0°$, for all the angles of polarization, Figure 6.17(a)-(c). However, for cross-polarization i.e. $\varphi = 90°$, lowering of RCS reduction is seen for incidence angle $\theta > 10°$ on either side of normal incidence. For a completely co-polarized wave i.e. $\varphi = 0°$, RCS reduction >10 dB is observed for almost all values of θ .

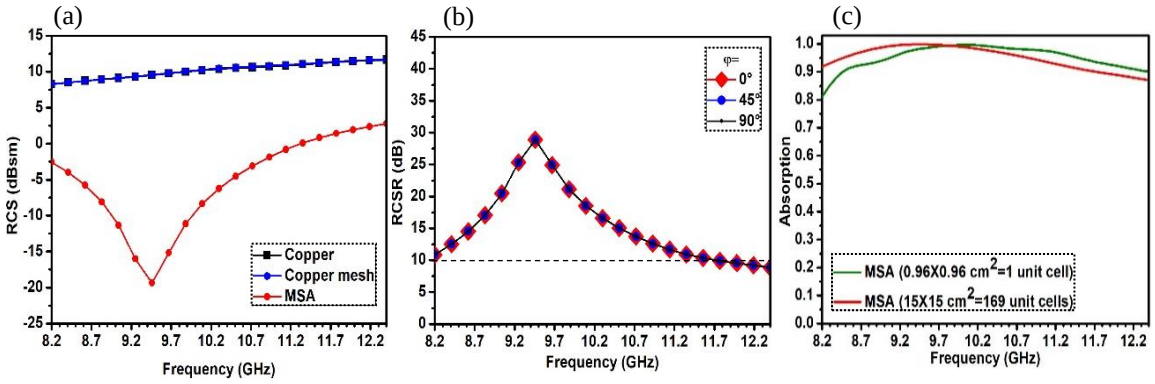

Figure 6.18 (a) Simulated monostatic RCS of copper plate, copper mesh and copper mesh backed OT-MSA. (b) Simulated monostatic RCS reduction at different polarization angles in copper mesh backed OT-MSA. (c) Simulated absorbance curves for copper mesh backed MSA with single unit cell and 169 unit cells.

Similar studies are conducted for monostatic RCS configuration. Copper plate and copper mesh shows alike RCS and plotted in Figure 6.18(a). The MSA shows a 10 dB reduction in RCS covering almost the entire X-band, Figure 6.18(b). Corresponding absorbance determined using equation (4.13) is drawn in Figure 6.18(c). A concurrence is observed with the absorption data simulated for unit cell using the Floquet port technique (section 4.5.3.) The RCS reduction for different polarization angles of incident waves are given in Table 6.6.

Table 6.6 Monostatic RCS performance of the copper mesh backed OT-MSA in reference to copper plate.

Incidence angle	Monostatic RCS reduction at different polarization angles		
	$\varphi = 0°$	$\varphi = 45°$	$\varphi = 90°$
$\theta = 0°$	> 30 dB	> 30 dB	> 30 dB

6.5.2 RCS measurement

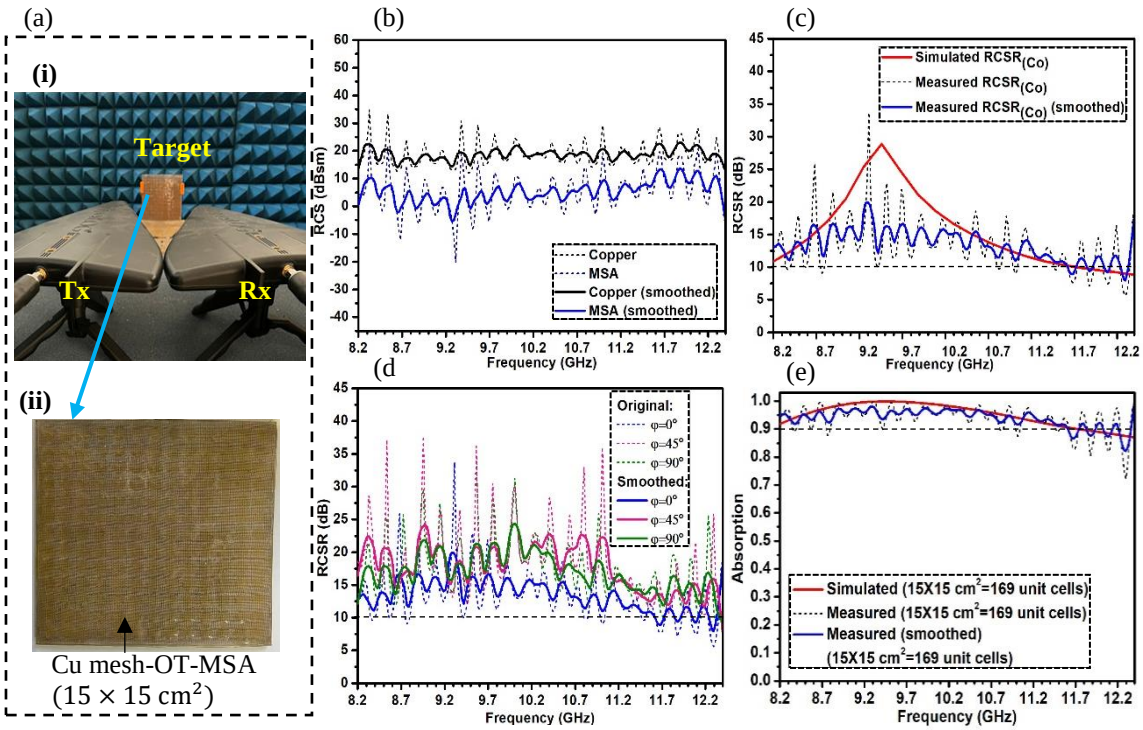

Figure 6.19 (a)(i) RCS measurement setup and (ii) copper mesh backed MSA sample. (b) Monostatic RCS of copper plate and copper mesh backed OT-MSA at normal incidence, (c) Monostatic RCSR in copper mesh backed OT-MSA in reference to copper plate for (c) co-polarized incidence and (d) different polarization angles. (e) Corresponding simulated and measured absorbance.

The monostatic RCS is measured using the setup referred in chapter IV, section 4.5.3, Figure 6.19(a)(i). For this a 15×15 cm^2 sized copper mesh backed OT-MSA is fabricated, Figure 6.19(a)(ii) and evaluated in reference to copper plate of same

dimension. Figure 6.19(b) plots the monostatic RCS. RCS reduction relative to copper plate is traced in Figure 6.19(c). RCSR ≥ 10 dB is observed for almost the entire X-band at all the polarization angles as obvious from the plots in Figure 6.19(d). Simulated and measured absorbance, Figure 6.19(e), are in good accordance showing 90% absorption in the range 8.2 – 11.7 GHz. The small variation in values could be attributed to near-field disturbances produced by close proximity of Tx and Rx antennas in the measurement setup.

6.6 ASSESSMENT OF COPPER MESH BACKED OT-MSA PERFORMANCE

Table 6.7 gives overall specifications of the developed DES gel OT-meta-structure absorber.

Table 6.7 Specifications of the optically transparent copper mesh backed MSA.

Absorber performance:							
MSA	**A_ω ≥90% BW (GHz)**	**RL (dB)**	**RF (GHz)**	**PA-T**	**IA-T**	**RCSR BW at X-band (GHz)**	**Temperature tolerance** (℃)
Copper mesh backed (Cu mesh-OT-MSA)	8.5-12.4	-26.39	10.04	±90°	±50°	4.2	-15 to 65

Other features:							
MSA	**Adhesion strength to back (Peel test)**	**Elongation at break without R-back (%)**	**O-T without R- back (%)**	**O-T with R-back (%)**	**UV-T (%)**	**WA (%)**	**ρ (g cm^{-3})**
Copper mesh back (Cu mesh-OT-MSA)	Elongation is 10% with a stress of 0.06 MPa	40	~80	~45	0	2.6	1.32 (with R-back) 1.19 (without R-back)

***Note*: A_ω**-absorption, BW- bandwidth, RL- reflection loss, RF- resonant frequency, O-T- optical transparency, R-reflecting, UV-T- ultraviolet transparency, WA-water absorption, ρ - density.

The developed copper mesh backed OT-MSA exhibits >90% absorption over 3.9 GHz range in X-band with optical transparency of ~45%. The copper mesh adheres properly to the urethane rubber matrix and the whole absorber shows sufficient flexibility. Water retention is almost negligible and they are light weighted.

Hence, the developed copper mesh backed OT-MSA prototype may find applications where adequate visible transparency and microwave shielding is desired.

6.7 INVESTIGATION OF SOLAR PANEL PERFORMANCE WITH OT-MSA

Solar panels are used for both civilian and military purposes across diverse sectors. Solar panels exhibit characteristics similar to those of metal in the microwave area [9, 10]. The reflection of microwave signals from a substantial array of solar panels, has the potential to disrupt wireless communication in close proximity. Additionally, these reflections augment the radar cross section (RCS) of the panels, making them more easily detectable which is undesirable, particularly in military contexts. As a result, concealment of solar panel reflections is desirable.

Metal backing in the solar panel makes it behave as a totally reflecting surface akin to copper plate/mesh at microwave frequencies, hence, the developed optically transparent DES gel MSA devoid of mesh can be used on the panel surface directly to evaluate its performance.

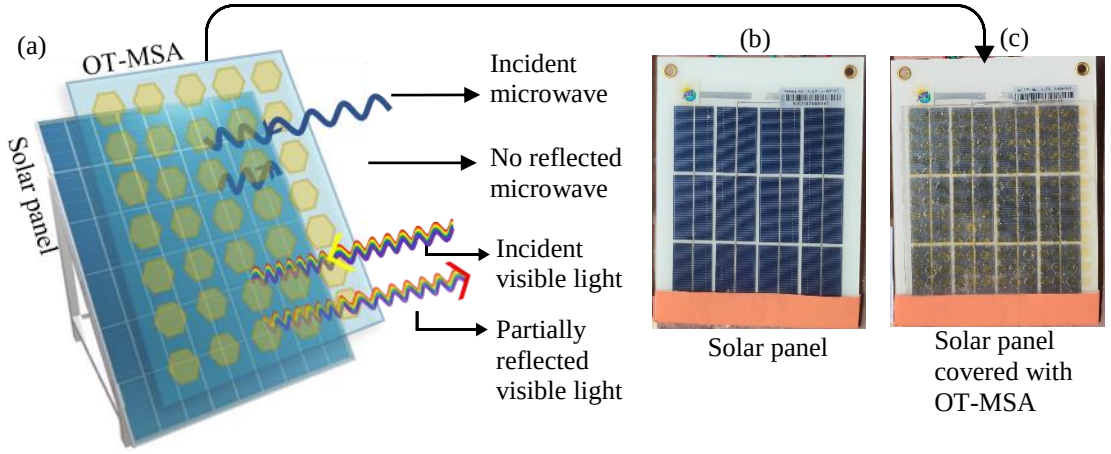

Figure 6.20 (a) Schematic of OT-MSA covered solar panel operating mechanism. (b) Photograph of (i) solar panel used and (ii) OT-MSA covered solar panel.

The schematic in Figure 6.20(a) illustrates the solar panel with MSA stacked on its top surface. Figure 6.20(b) shows the photograph of (i) solar panel and (ii) DES gel OT-MSA covered panel. Commercially available solar panel (Make: Surcle) of size 15 × 15 cm^2 is considered for the study conducted here. The fabricated DES gel OT-MSA is sized to cover the entire panel. Tests are carried out to determine RCS and conversion efficiency of the solar panel is evaluated before and after employing the OT-MSA.

6.7.1 RCS performance

The placement of the panel with and without OT-MSA in the RCS measurement setup is shown in Figure 6.21(a). The graphs in Figure 6.21(b) reveals that the RCS of the solar panel is almost equal to that of copper. A lowering of RCS is observed when DES gel OT-MSA is placed over the solar panel with a 10 dB RCSR ranging over the entire X-band, Figure 6.21(c).

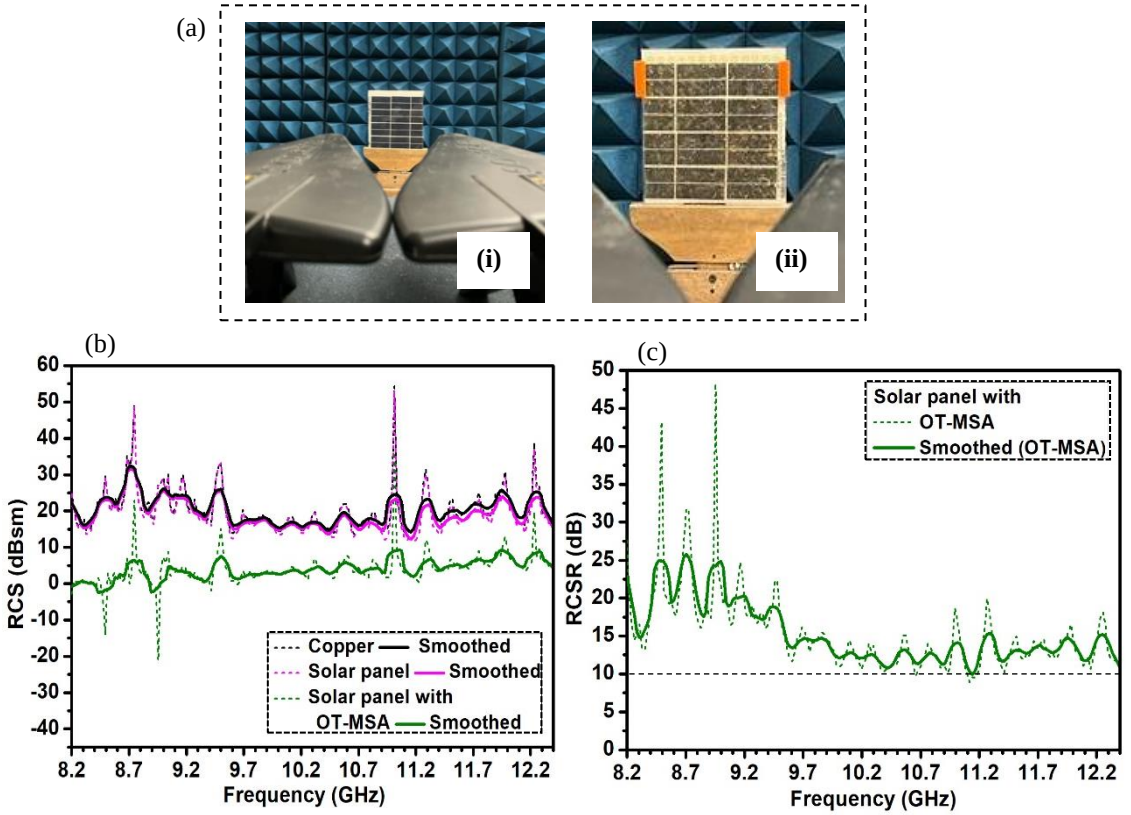

Figure 6.21 (a) Monostatic RCS measurement setup with (i) solar panel and (ii) OT-MSA covered solar panel (b) Monostatic RCS of copper plate, solar panel and OT-MSA covered solar panel. (c) Monostatic RCSR of OT-MSA covered solar panel.

6.7.2 Light conversion efficiency performance

The solar panel performance is analyzed by determining light conversion efficiency using the relation,

$$\eta_c\ (\%) = \frac{P_{out}}{I_r \times A} \times 100 \qquad (6.1)$$

Where, η_c is the conversion efficiency, P_{out} is the output power (W) of the solar panel, I_r is the radiant flux incident on solar panel (Wm^{-2}) and A is the working area of the

solar panel which is set as 0.15 × 0.15 m^2.

Experiments are conducted both inside the lab i.e. indoor, Figure 6.22(a) and outdoor under direct sunlight, Figure 6.22(b).

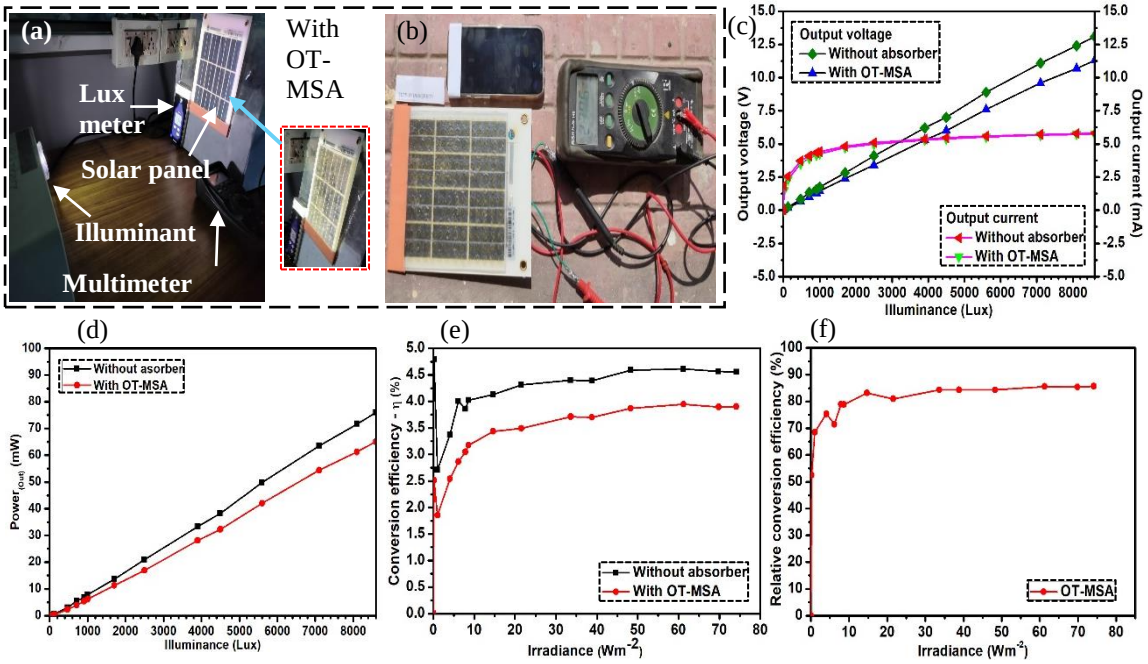

Figure 6.22 (a) Indoor solar panel performance measurement setup. (b) Outdoor solar panel performance measurement setup. Output (c) current, voltage and (d) power at different illuminance intensity. (e) Conversion efficiency of solar panel with and without the OT-MSA cover. (f) Relative conversion efficiency of OT-MSA with reference to solar panel.

Indoor performance:

The solar panel is illuminated with a light source at a fixed distance of 40 cm from the source. The intensity of light is varied from 0 to 8600 lux and corresponding I-V characteristics is recorded. The output current, voltage values and corresponding output power as a function of illuminance (I_l) are plotted for each configuration in Figure 6.22(c) and (d). Conversion efficiency with irradiance is plotted in Figure 6.22(e). Here, irradiance (Wm^{-2}) is calculated using equation $I_r = \frac{1}{116} I_l$ [27].

Increase in illuminance intensity enhances the output power of the solar panel. The relative conversion efficiency (R_{η_c}) of solar panel, Figure 6.22(f), sheathed with OT-MSA is found to be lowered by 15 to 20% in reference to direct illumination of the solar panel.

Outdoor performance:

Here, the measurements are directly taken under sunlight, (on 5.08.2023, 2:00 P.M (IST), at 26.6988◦N and 92.8325◦E), Figure 6.22(b). The irradiance (Wm^{-2}) is computed using equation $I_r = \frac{1}{122} I_l$ [27]. The obtained values are tabulated in Table 6.8.

The outdoor performance follows the indoor performance trend. It is observed that enhanced outdoor intensity leads to an increased output power.

Table 6.8 Outdoor performance of solar panel before and after OT-MSA cover.

Sample	**Temperature (°C)**	**Intensity (Lux)**	**Irradiance (Wm^{-2})**	**I (mA)**	**V (V)**	**Power (W)**	**η (%)**	**R_η (%)**
Solar panel	35-40	85,000	696.72	299.6	7	2.0972	13.37	100
Solar panel covered with OT-MSA	35-40	85,000	696.72	244.3	6.87	1.6570	10.71	80.03
Note: I-current, V-voltage, η_c-conversion efficiency and R_{η_c}- relative conversion efficiency.								

6.7.3 Solar panel performance analysis

The flexible urethane matrix OT-MSA adheres to the solar panel surface without need of any adhesive or external mounting. The solar panel when blanketed with the DES gel OT-MSA shows above 10 dB RCS reduction over the entire working band with a nominal effect on its light conversion efficiency. For outdoor measurements more than 80% relative conversion efficiency-R_{η_c} is achieved. The efficiency is in line with the optical transparency measurement carried out for the OT-MSA stripped out of copper mesh as tabulated in Table 6.7. The ambient temperature of the system reaches around 35-40°C , which is within the temperature tolerance range of the OT-MSA (refer Table 6.7). As per the data sheet, the solar panel can get as hot as 65°C and the OT-MSA retains absorption performance upto this temperature. In addition, the OT-MSA blocks the UV radiation which is reported to have detrimental effect on solar panels [28, 29].

The copper mesh backed OT-MSA as anticipated reduces the original panel conversion efficiency by 55-57%, Figure 6. 23, which is proportional to its optical transparency limit as observed in Figure 6.12 (c).

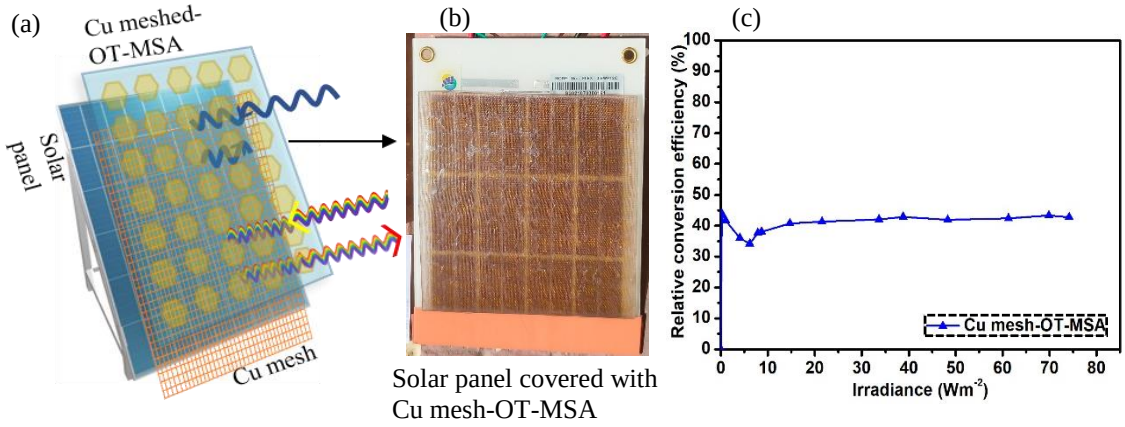

Figure 6.23 Copper mesh backed OT-MSA covered solar panel (a) schematic of operating mechanism, (b) photograph and (c) relative conversion efficiency in reference to solar panel.

6.8 CHAPTER SUMMARY

An effective optically see-through and microwave opaque shield prototype is fabricated using optically transparent urethane rubber matrix which embeds transparent hexagonal-prism shaped conducting DES gel subwavelength resonating structures. The conventional PEC reflecting back is replaced by copper mesh to obtain a standalone MSA tile (15×15 cm^2). The six-fold symmetric subwavelength resonator design and choice of the materials give polarization independent wide band performance with reduced RCS. The standalone copper mesh backed OT-MSA can be used on non-metallic targets, with some compromise on optical visibility.

The designed structure devoid of copper mesh can be readily mounted on metallic targets accomplishing good absorption. Low RCS in X-band and 80% optical transparency finds an application on camouflaging solar panels without much effecting its performance and aesthetics.

REFERENCES

[1] Reghunadhan, A. and S. Thomas. Polyurethanes: structure, properties, synthesis, characterization, and applications. *Polyurethane polymers*, 1-16, Elsevier. 2017.

[2] Clemitson, I.R. Castable polyurethane elastomers. CRC Press, 2008.

[3] Tian, S., et al. Transparent broadband wide-angle polarization-insensitive metasurface absorber for microwave antireflection. In *2019 IEEE MTT-S International Wireless Symposium (IWS)*, 2019 pages 1-3, 2019. IEEE.

[4] Venkatarayalu, N., et al. Effect of resistivity of ITO thin film when used in transparent checkerboard surfaces for RCS reduction. In *2017 Progress in Electromagnetics Research Symposium-Fall (PIERS-FALL)*, 2017 pages 473-476, 2017. IEEE.

[5] Zhang, L., et al., Broadband transparent absorber based on indium tin oxide-polyethylene terephthalate film. *IEEE access*, 7: 137848-137855, 2019.

[6] Zhou, Q., et al., Optically transparent and flexible broadband microwave metamaterial absorber with sandwich structure. *Applied Physics A*, 125: 1-8, 2019.

[7] Xiong, Y., et al., Ultra-thin Optically Transparent Broadband Microwave Metamaterial Absorber Based on Indium Tin oxide. 2022.

[8] Lai, S., et al., A high-performance ultra-broadband transparent absorber with a patterned ITO metasurface. *IEEE Photonics Journal*, 14(3): 1-7, 2022.

[9] Kong, X., et al., Transparent metamaterial absorber with broadband radar cross-section (RCS) reduction for solar arrays. *IET Microwaves, Antennas & Propagation*, 14(13): 1580-1586, 2020.

[10] Li, S., et al., Ultrathin optically transparent metamaterial absorber for broadband microwave invisibility of solar panels. *Journal of Physics D: Applied Physics*, 55(4): 045101, 2021.

[11] Lee, I.-G., et al., Design of an optical transparent absorber and defect diagnostics analysis based on near-field measurement. *Sensors*, 21(9): 3076, 2021.

[12] Tayde, Y., et al., An optically transparent and flexible microwave absorber for X and Ku bands application. *Microwave and Optical Technology Letters*, 62(5): 1850-1859, 2020.

[13] Grande, M., et al., Optically transparent microwave screens based on engineered graphene layers. *Optics Express*, 24(20): 22788-22795, 2016.

[14] Grande, M., et al., Reconfigurable and optically transparent microwave absorbers based on deep eutectic solvent-gated graphene. *Scientific reports*, 9(1): 1-9, 2019.

[15] Wang, X.-R., et al., Optically transparent microwave shielding hybrid film composited by metal mesh and graphene. *Prog. Electromagn. Res.*, 170: 187-197, 2021.

[16] Yi, D., X. Wei, and Y. Xu. Experimental demonstration of transparent microwave absorber based on graphene. In *2016 IEEE MTT-S International Wireless Symposium (IWS)*, 2016 pages 1-4, 2016. IEEE.

[17] Lu, W.B., et al., Flexible and optically transparent microwave absorber with wide bandwidth based on graphene. *Carbon*, 152: 70-76, 2019.

[18] Min, P., et al., Optically transparent flexible broadband metamaterial absorber based on topology optimization design. *Micromachines*, 12(11): 1419, 2021.

[19] Baron, T., et al., Design of metallic mesh absorbers for high bandwidth electromagnetic waves. *Progress In Electromagnetics Research C*, 8: 135-147, 2009.

[20] Bulut, F., et al. Electromagnetic shielding behavior of different metallic wire-meshes and thin metal plate. In *2017 IV International Electromagnetic Compatibility Conference (EMC Turkiye)*, 2017 pages 1-3, 2017. IEEE.

[21] Casey, K.F., Electromagnetic shielding behavior of wire-mesh screens. *IEEE transactions on Electromagnetic Compatibility*, 30(3): 298-306, 1988.

[22] Raj, C.D., M. Ramyasree, and V.S. Kumar. Analysis of wire mesh screen for shielding effectiveness in different frequency ranges. In *2011 International Conference on Computer, Communication and Electrical Technology (ICCCET)*, 2011 pages 198-203, 2011. IEEE.

[23] Zimmer, S., et al., Modeling Electrical Conductivity of Metal Meshes for Predicting Shielding Effectiveness in Magnetic Fields of Wireless Power Transfer Systems. *Electronics*, 11(14): 2156, 2022.

[24] Sheokand, H., et al., Transparent broadband metamaterial absorber based on resistive films*. Journal of applied physics*, 122(10), 2017.

[25] Min, P., et al., Transparent ultrawideband absorber based on simple patterned resistive metasurface with three resonant modes*. Optics express*, 28(13): 19518-19530, 2020.

[26] Yasin, T. Transparent antennas for solar cell integration. Utah State University, 2013.

[27] Michael, P.R., D.E. Johnston, and W. Moreno, A conversion guide: Solar irradiance and lux illuminance*. Journal of Measurements in Engineering*, 8(4): 153-166, 2020.

[28] Bora, B., et al., Effect of UV irradiation on PV modules and their simulation in newly designed site-specific accelerated ageing tests*. Solar Energy*, 253: 309-320, 2023.

[29] Perrakis, G., et al., Ultraviolet radiation impact on the efficiency of commercial crystalline silicon-based photovoltaics: a theoretical thermal-electrical study in realistic device architectures*. OSA Continuum*, 3(6): 1436-1444, 2020.